Estimation of the Optimal Maximum Beam Angle and Angular Increment for Normal and Shear Strain Estimation

Min Rao*, *Student Member, IEEE*, and Tomy Varghese, *Senior Member, IEEE*

***Abstract*—In the current practice of ultrasound elastography, only the axial component of the displacement vector is estimated and used to produce strain images. A method was recently proposed by our group to estimate both the axial and lateral components of a displacement vector using RF echo signal data acquired along multiple angular insonification directions of the ultrasound beam. Previous work has demonstrated that it is important to choose appropriate values for the maximum beam angle and angular increment to achieve optimal performance with this technique. In this paper, we present error propagation analysis using the least-square fitting process for the optimization of the angular increment and the maximum beam steered angle. Ultrasound simulations are performed to corroborate the theoretical prediction of the optimal values for the maximum beam angle and angular increment. Selection of the optimal parameters depends on system parameters, such as center frequency and aperture size. For typical system parameters, the optimal maximum beam angle is around 10° for axial strain estimation and around 15° for lateral strain estimation. The optimal angular increment is around 4°–6°, which indicates that only five to seven beam angles are required for this strain-tensor estimation technique.**

***Index Terms*—Elasticity, elasticity imaging, elastogram, elastography, shear strain, strain, strain tensors, stiffness, ultrasound.**

I. Introduction

In RECENT years, ultrasound-based strain imaging has received considerable interest for use in the diagnosis of both focal and diffuse diseases [1]–[8]. Elastography is an imaging modality that is based on mapping local internal strains that biological tissue experience after a quasi-static or dynamic compression. In this technique, local strains are typically estimated along the axial direction corresponding to the beam propagation axis by taking the gradient of the tissue displacement following a uniaxial compression (generally in the direction of beam propagation) [1], [2], [9], [10]. Local tissue displacements along the beam direction are calculated using time-delay estimation techniques [11]. Lateral (perpendicular to the beam propagation axis and in the scan plane) and elevational (perpendicular to the beam propagation axis and the scan plane) displacements are usually not estimated in elasticity imaging. However, all the components of the strain tensor and displacement vector are required to characterize the deformation following compression since tissue motion inevitably occurs in three dimensions [12], [13]. Because the components of the strain tensor are coupled, accurate estimations of all components are necessary for a complete visualization of the strain incurred in tissue. In addition, without these components, other important parameters such as shear strains and the Poisson's ratio cannot be estimated. Knowledge of the strain tensors and Poisson's ratio is also necessary for Young's modulus reconstruction algorithms [14], [15].

Previous research in the estimation of 3-D components of the tissue displacement vector for strain imaging has been reported in the literature [16], [17]. Lubinski *et al.* [16] obtained lateral displacement estimates utilizing the assumption of tissue incompressibility. Lateral displacements were computed using the higher precision axial displacement estimates and assuming a Poisson's ratio of 0.495. However, the incompressibility assumption may not hold in some tissues, for example, lung tissue with a Poisson's ratio of 0.3 [18] and cartilage with a Poisson's ratio of 0.17 [19]. In addition, the Poisson's ratio may not be constant, such as for poroelastic tissue, especially when edema is present [20], [21]. Konofagou and Ophir [17] proposed the simultaneous estimation of both axial and lateral displacements and strains using a precision tracking algorithm based on weighted interpolation between neighboring RF A-lines in the lateral direction, along with an iterative correction of lateral and axial displacements. They applied a number of cross-correlation and correction stages for axial and lateral displacements. However, the extensive lateral interpolation between RF A-lines and the iterative nature of the algorithm increases its computational complexity.

Our group recently proposed a method to estimate components of a displacement vector using RF echo signal data acquired along multiple angular insonification directions of the ultrasound beam [22], [23]. Displacements at each spatial location in the compressed medium are measured along each beam direction using time-delay estimation techniques [11]. A linear model of the relationship between these directional displacements and components of the actual displacement vector is constructed. Different components of the displacement vector are then estimated using a least squares solution [22], [23]. The strain-tensor components are computed from the gradient of the corresponding displacement vector components. This strain-tensor estimation method can reduce noise artifacts in axial strain images and obtain lateral and shear strain images at the same time, but at

Manuscript received January 24, 2008; revised May 2, 2008. First published September 26, 2008; current version published April 15, 2009. This work was supported in part by the Komen Foundation under Grant BCTR0601153. *Asterisk indicates corresponding author.*

*M. Rao is with the University of Wisconsin, Madison, WI 53706 USA (e-mail: min.mrao@gmail.com).

T. Varghese is with the University of Wisconsin, Madison, WI 53706 USA (e-mail: tvarghese@wisc.edu).

Color versions of one or more of the figures in this paper are available online at http://ieeexplore.ieee.org.

Digital Object Identifier 10.1109/TBME.2008.2005907

the expense of the additional processing time required for displacement estimations along the angular directions. The number of angular datasets depends on two factors: the angular increment and the maximum angle used in this technique. Generally, increasing the maximum angle reduces the strain variance and improves the elastographic SNR (SNRe). However, increased decorrelation noise artifacts are present for the displacement obtained over larger insonification angles [24]. So, there exists an optimal value for the maximum angle used in the strain-tensor estimation technique. In addition, for a fixed maximum angle, the most efficient use of processing time would occur if the data acquired from the different angular directions were statistically independent. Thus, it is important to choose appropriate values for the maximum beam angle or angular increment to achieve optimal performance with this technique.

In this paper, we present a derivation of error propagation analysis through the least-square fitting process used in our technique. The variance of the final axial and lateral displacement estimates is expressed as a function of the beam angle. Ultrasound simulations are performed to corroborate the theoretical prediction of the optimal value of the maximum beam angle and angular increment used in this technique.

II. Theory

In our method, the displacement vector at each pixel on the zero-angle grid is estimated using a least squares approach. The relationship between the actual displacement vector and the measured angular displacement is given by [22]

$$\bar{q} = A\bar{d} + \bar{n} \tag{1}$$

where

$$\bar{q} = \begin{bmatrix} q_1 \\ q_2 \\ \vdots \\ q_m \end{bmatrix}, \qquad A = \begin{bmatrix} \cos\,\theta_1 & \sin\,\theta_1 \\ \cos\theta_2 & \sin\,\theta_2 \\ \vdots & \vdots \\ \cos\,\theta_m & \sin\,\theta_m \end{bmatrix},$$

$$\bar{d} = \begin{bmatrix} d_z \\ d_x \end{bmatrix}, \qquad \text{and} \qquad \bar{n} = \begin{bmatrix} n_{\theta_1} \\ n_{\theta_2} \\ \vdots \\ n_{\theta_m} \end{bmatrix}.$$

The variable q_i represents an observation of the displacement vector $\bar{d}$ at beam angle θ_i for $i = 1, \ldots, m$, where m is the total number of beam steering angles and n_{θ_i} is the noise in the observation at angle θ_i. For simplicity, the noise in the angular strain estimates is assumed to be similar for all measurements. The variables *dz* and *dx*, respectively, denote the axial and lateral displacements for the zero-angle condition. We can minimize the squared error between the measurement $\bar{q}$ and the linear model $A\bar{d}$ with respect to $\bar{d}$ to estimate the value of $\bar{d}$. The solution is the least squares solution [25], which is given by

$$\tilde{d} = \left(A^T A\right)^{-1} A^T \bar{q} \tag{2}$$

where $\tilde{d} = [\tilde{d}_z,\ \tilde{d}_x]'$ is a vector whose elements represent estimates of the axial and lateral displacements.

We start with computing the error propagation through the least-square fitting process. First, we derive explicit expressions of the axial and lateral displacements from (2)

$$A^T A = \begin{bmatrix} \sum_j \cos^2\,\theta_j & \sum_j \sin\,\theta_j\,\cos\,\theta_j \\ \sum_j \sin\,\theta_j\,\cos\,\theta_j & \sum_j \sin^2\theta_j \end{bmatrix}. \tag{3}$$

The inverse matrix of $A^{\mathrm{T}} A$ can be written as

$$\left(A^T A\right)^{-1} = \frac{1}{|A^T A|} \begin{bmatrix} \sum_j \sin^2\,\theta_j & -\sum_j \sin\,\theta_j\,\cos\,\theta_j \\ -\sum_j \sin\,\theta_j\,\cos\,\theta_j & \sum_j \cos^2\,\theta_j \end{bmatrix} \tag{4}$$

where $|A^T A|$ is the determinant of $A^T A$. So, we can obtain axial and lateral displacement estimates, which are linear combinations of the angular displacements q_i

$$d_z = \sum_i c_{1i} q_i \qquad d_x = \sum_i c_{2i} q_i \tag{5}$$

where c_1 and c_2 are functions of θ, and can be derived from (2) as

$$c_{1i} = \frac{\cos\,\theta_i \sum_j \sin^2\,\theta_j - \sin\,\theta_i \sum_j \sin\,\theta_j\,\cos\,\theta_j}{\sum_j \sin^2\,\theta_j \sum_j \cos^2\,\theta_j - \left(\sum_j \sin\,\theta_j\,\cos\,\theta_j\right)^2}$$

$$c_{2i} = \frac{\sin\,\theta_i \sum_j \cos^2\,\theta_j - \cos\,\theta_i \sum_j \sin\,\theta_j\,\cos\,\theta_j}{\sum_j \sin^2\,\theta_j \sum_j \cos^2\,\theta_j - \left(\sum_j \sin\,\theta_j \cos\,\theta_j\right)^2}. \tag{6}$$

If we consider only the case with symmetrical negative and positive angles, the summation terms of $\sum_j \sin\,\theta_j \cos\,\theta_j$ in the previous equations become zero, and c_1 and c_2 can be simplified as follows:

$$c_{1i} = \frac{\cos\,\theta_i}{\sum_j \cos^2\,\theta_j} \qquad c_{2i} = \frac{\sin\,\theta_i}{\sum_j \sin^2\,\theta_j}. \tag{7}$$

Hence, the estimation of the axial and lateral displacements can be written as

$$d_z = \frac{\sum_i \cos\,\theta_i q_i}{\sum_i \cos^2\,\theta_i} \qquad d_x = \frac{\sum_i \sin\,\theta_i q_i}{\sum_i \sin^2\,\theta_i}. \tag{8}$$

The variance for *dz* and *dx* can then be derived as follows:

$$\sigma_{dz}^2 = \sum_i \sum_j c_{1i} c_{1j} \mathrm{cov}\,(q_i, q_j)$$

$$\sigma_{dx}^2 = \sum_i \sum_j c_{2i} c_{2j} \mathrm{cov}\,(q_i, q_j) \tag{9}$$

where $\mathrm{cov}(q_i, q_j)$ denotes the covariance between the angular displacement estimates at insonification angle θ_i and θ_j, given by

$$\mathrm{cov}(q_i, q_j) = \rho_{ij} \sigma_{qi} \sigma_{qj} \tag{10}$$

where σ_{qi} is the standard deviation of the angular displacement estimates and can be obtained from the variance of the angular displacement estimates and is given in [26], (11) as shown at the bottom of the next page, where γ, δ, μ, and η are thresholds [26], s denotes the strain, T is the axial window length in units of time, B is the bandwidth, f_c is the center frequency, and the SNR term

represents the contribution only due to electronic noise (SNR_S). SNR_C incorporates both the electronic noise and the decrease in SNR caused by signal decorrelation, given as [26]

$$\mathrm{SNR}_C = \frac{\mathrm{SNR}_S \mathrm{SNR}_\rho}{1 + \mathrm{SNR}_S + \mathrm{SNR}_\rho} \tag{12}$$

where $\mathrm{SNR}_\rho = \rho(\theta_i)/1 - \rho(\theta_i)$ and $\rho(\theta_i)$ is the correlation coefficient between the pre- and postcompression RF signals acquired at beam angle θ_i, given as [24]

$$\rho(\theta_i) = \sqrt{\frac{2a}{a^2+1}} \times \exp\left\{-\frac{\cos^2\theta_i}{4}\left[\frac{(x_{01}-x_{02})^2}{\sigma_x^2} + \frac{(z_{01}-az_{02})^2}{\sigma_z^2}\right]\right\} \times \exp\left(-\frac{\sigma_z^2\pi^2 f^2}{\cos^2\theta_i}\right)_{f=1-a^2/a^2\lambda_0}. \tag{13}$$

The parameter a is the compression or strain factor that scales the tissue scattering function defined in terms of the actual applied tissue compression ε, $a = 1/(1-\varepsilon) \sim 1+\varepsilon$ for $\varepsilon \ll 1$. (x_{01}, z_{01}) and (x_{02}, z_{02}) are the coordinates of the positions where the pre- and postcompression RF signals are acquired. σ_x and σ_z are the widths of the lateral and axial beam point spread function, respectively, which are assumed to be Gaussian profiles defined by $p_z(z) = \exp(-z^2/2\sigma_z^2)$ and $p_x(x) = \exp(-x^2/2\sigma_x^2)$, and λ_0 is the wavelength at the center frequency.

The term ρ_{ij} in (10) is the correlation coefficient between the angular displacement estimates at angles θ_i and θ_j. Since the angular displacements are derived from angular pre- and postcompression RF signals, it is natural to look for ρ_{ij} through the correlation between angular RF signals acquired from beam angles θ_i and θ_j. We have developed a theoretical formalism that approximates $\rho_{\mathrm{RF}}(\theta_i,\ \theta_j)$, the correlation between RF signals acquired from any two beam angles [27]

$$\rho_{\mathrm{RF}}(\theta_i,\theta_j) = 2\sqrt{\frac{a\cos^2\theta_i\cos^2\theta_j}{(\cos^2\theta_i+\cos^2\theta_j)(a^2\cos^2\theta_i+\cos^2\theta_j)}}F_1F_2 \tag{14}$$

where F_1 and F_2 can be written as

$$F_1 = \exp\left[-\frac{\cos^2\theta_i\cos^2\theta_j}{2\sigma_x^2(\cos^2\theta_i+\cos^2\theta_j)}(x_{01}-x_{02})^2\right] \times \exp\left(\frac{-2\pi^2\sigma_x^2 f^2}{\cos^2\theta_i+\cos^2\theta_j}\right)_{f=2b/z_{01}\lambda_0} \tag{15}$$

$$F_2 = \exp\left[-\frac{\cos^2\theta_i\cos^2\theta_j}{2\sigma_z^2(a^2\cos^2\theta_i+\cos^2\theta_j)}(z_{01}-az_{02})^2\right] \times \exp\left(\frac{-2\pi^2\sigma_z^2 a^2 f^2}{a^2\cos^2\theta_i+\cos^2\theta_j}\right)_{f=1-a^2/a^2\lambda_0} \tag{16}$$

where (x_{01}, z_{01}) and (x_{02}, z_{02}) are the coordinates of the positions where the pre- and postcompression RF signals are acquired, b is the distance between the two apertures of the transducer given by $b = z_{01}(\tan\theta_i - \tan\theta_j)$. It is possible to derive ρ_{ij} from $\rho_{\mathrm{RF}}(\theta_i,\ \theta_j)$; however, the derivation is complicated. For the sake of simplicity, we use $\rho_{\mathrm{RF}}^2(\theta_i,\theta_j)$ to approximate ρ_{ij}.

Thus, the lower bound on the variance of the axial and lateral displacements can be obtained by substituting (11) and (14) into (9). From the definition of the strain tensors, we can estimate the lower bound on the variance of the axial and lateral strain estimates using the following relationship:

$$\sigma_{sz}^2 \geq \frac{2\sigma_{dz}^2}{Z\,\Delta z} \qquad \sigma_{sx}^2 \geq \frac{2\sigma_{dx}^2}{X\,\Delta x} \tag{17}$$

where σ_{sz}^2 and σ_{sx}^2 are the variances of axial strain and lateral strain estimates, respectively, X denotes the lateral beam width, which is assumed to be $2\sigma_x$, Δx the beam spacing, and Z and Δz are the window length and window separation in the axial direction.

III. Simulations

A. Method

Numerical simulations are used to verify the theoretical derivation presented in this paper. Ultrasound RF echo signals at different insonification angles before and after an applied compression of the tissue-mimicking numerical phantom were obtained using an ultrasound simulation program developed by Li and Zagzebski [28]. The conditions simulated for the acquisition of RF signals at different beam steering angles is shown in Fig. 1. A linear array transducer was modeled, which consisted

$$\sigma_{qi}^2 \geq \begin{cases} \dfrac{(sT)^2}{12}, & (BT)\,\mathrm{SNR}_C < \gamma \\ \text{Threshold } \gamma < (BT)\,\mathrm{SNR}_C < \delta & \\ \dfrac{18f_c^2}{\pi^2 T(B^5+12B^3f_c^2)}\left[\dfrac{1}{\rho(\theta_i)^2}\left(1+\dfrac{1}{\mathrm{SNR}^2}\right)^2-1\right], & \delta < (BT)\,\mathrm{SNR}_C < \mu \\ \text{Threshold } \mu < (BT)\,\mathrm{SNR}_C < \eta & \\ \dfrac{3}{2\pi^2 T(B^3+12Bf_c^2)}\left[\dfrac{1}{\rho(\theta_i)^2}\left(1+\dfrac{1}{\mathrm{SNR}^2}\right)^2-1\right], & \eta < (BT)\,\mathrm{SNR}_C \end{cases} \tag{11}$$

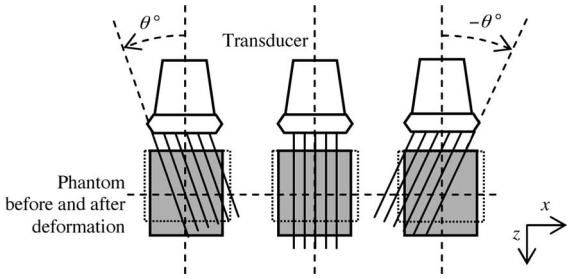

Fig. 1. Schematic diagram of the angular insonfication method for strain-tensor estimation. Beam steering using a linear array transducer is used from -25° to 25° with a minimum angular increment of 1°. RF signals are generated for each beam angle before and after an applied compression of the tissue-mimicking numerical phantom.

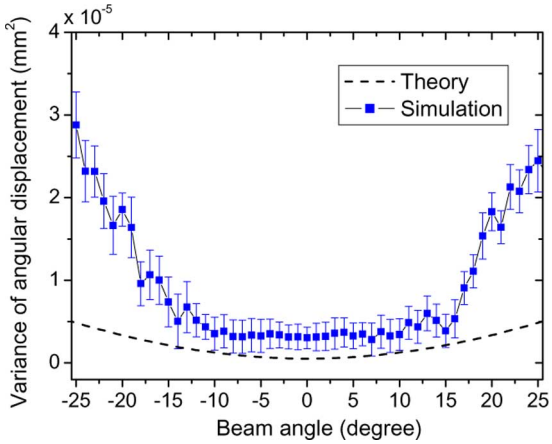

Fig. 2. Variance of the angular displacement estimates versus the beam angle.

of 0.1 × 10 mm elements with a 0.1-mm center-to-center element separation. Each beam line was formed using 128 consecutive elements. Beam steering for the linear array transducer was simulated by selecting appropriate time delays for each element that determines the focal point and steering angle for the beam. In our simulation, beam steering was applied from -25° to 25° with a minimum angular increment of 1°. The incident pulses were modeled to be Gaussian shaped with an 8-MHz center frequency and a -6 dB bandwidth of 100%. We set the transmit focus at 30 mm, and dynamic focusing was utilized on receive. The elevational focus was set at 60 mm. The sampling frequency utilized was 52 MHz.

A uniformly elastic phantom was simulated by modeling a random distribution of 50-μm polystyrene beads with an average concentration of 9.7 per mm^3 in a medium (to simulate Rayleigh scattering statistics) that has a speed of sound of 1540 m/s. The attenuation of the phantom was set to zero so that the signal intensity would be uniform for all depths. The modeled phantom dimensions were 40 (width) × 40 (height) × 10 mm (thickness). After calculating RF signals for each of the insonification angles as shown in Fig. 1, the phantom was deformed by a uniaxial compression (1% of the phantom height) in the z-direction, with the top surface of the phantom fixed. The displacement of each scatterer in the phantom was calculated using the finite-element analysis (FEA) software (ANSYS, Inc., Canonsburg, PA). The Poisson's ratio of the modeled phantom was set to 0.495, and plane-strain conditions were assumed. The new scatterer positions were used when calculating the postcompression echo signals at each insonification angle. The strain-tensor estimation algorithm [22], [23] was then applied to the pre- and postcompression angular RF datasets, and results were compared to the theoretical predictions derived in this paper.

B. Results

Fig. 2 presents a comparison between the theoretical prediction and simulation results for the variance of the angular displacement estimates as a function of the beam angle. For the simulation results, angular displacements were obtained by applying a 1-D normalized cross-correlation algorithm [1] to the simulated pre- and postcompression angular RF datasets using a 3-mm window size and 75% overlap between consecutive windows. Linear interpolation was utilized for image registration of the angular displacement data to a Cartesian spatial grid. The variance was then calculated using a rectangular region of interest (ROI) with dimensions of 2 × 2 mm at the center of angular displacement maps. To eliminate the effect of variation of angular displacement at different locations, the angular displacement estimates were detrended by ideal angular displacements, obtained using FEA simulations before computing the variance of angular displacement. The error bars denote the standard deviation of the mean–variance estimates over 12 independent datasets, which were obtained using 12 independent realizations of the ultrasound simulation program with randomly distributed tissue scatterers. The theoretical prediction, obtained by computing (11)–(13), is plotted as the dashed line. An increased variance is observed at larger beam steering angles, as shown in Fig. 2. This is because angular displacement estimates obtained when the beam angle relative to the direction of compression is large suffer from significant decorrelation of the pre- and postcompression RF echo signals. As illustrated in the figure, theoretical predictions underestimate the variance of angular displacements, especially at large beam angles ($>15^\circ$). This is because the theoretical model assumes that the displacement is accurately tracked [24], while the simulation results contain errors in the displacement estimates due to signal decorrelation effects, which are more pronounced at large beam steering angles [29]. Another reason for the discrepancy between theory and simulation is that the effective aperture may change slightly during the beam-steering process while the theoretical model does not take this effect into account.

Fig. 3 illustrates examples of axial (top) and lateral (bottom) displacement images of the simulated uniform phantom obtained by applying the strain-tensor estimation algorithm [22], [23] to the angular displacement estimates. Units of the displacement estimated are in millimeters. Results for different values of the maximum angle and angular increment are compared. Note that for the axial displacement computed, the images are quite smooth, and the maximum angle and angular increment have little impact on the image quality. The lateral displacement,

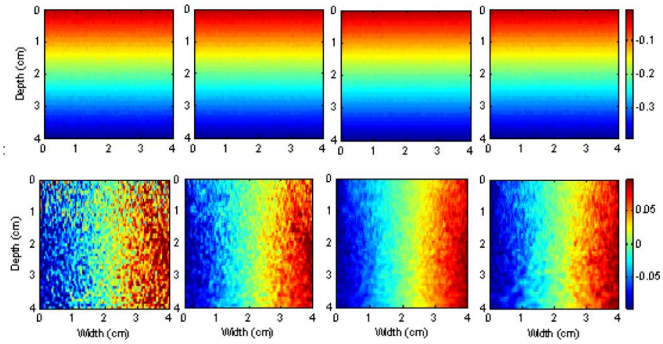

Fig. 3. Axial and lateral displacement images obtained using different values of maximum angle and angular increment. The unit of the displacement is millimeters. (a) $\theta_{\max} = 3°$, $\Delta\theta = 1°$. (b) $\theta_{\max} = 9°$, $\Delta\theta = 1°$. (c) $\theta_{\max} = 15°$, $\Delta\theta = 1°$. (d) $\theta_{\max} = 15°$, $\Delta\theta = 3°$.

however, is quite noisy as observed for a maximum angle of 3°, as shown in Fig. 3(a). Observe that as the maximum angle used in the strain-tensor estimation algorithm increases, the image quality of the lateral displacement is also improved. Also note that similar results are obtained when using an angular increment of 3° as compared to the results for an angular increment of 1°, as shown in Fig. 3(c) and (d).

Fig. 4 presents plots of the variance of the axial displacement versus the maximum angle and the angular increment. For the simulation results, the variance values were computed over a rectangular ROI with dimensions of 4 (width) × 1 mm (height) at the center of axial displacement images. The error bars represent the standard deviation obtained over 12 independent datasets. The angular increment used in the plot on the top was 1°, while the maximum angle used in the plot on the bottom was 12°. As illustrated in the figure, the theoretical prediction is lower than simulation results. This discrepancy can be explained as follows. First, our model underestimates the variance of the angular displacement, as shown in Fig. 2. Second, in our model, we use the correlation between pre- and postcompression RF signal acquired from two different beam angles to approximate the correlation between the angular displacement estimates at these two angles. The use of this approximation may lead to a small numerical discrepancy. Finally, the theoretical prediction of the displacement variance is estimated at a single position in the phantom, while the simulation results were computed over a small ROI in the displacement image. This may also lead to some differences between theoretical and simulation results. Nevertheless, the theoretical curve and simulation results follow a similar trend against the maximum angle and versus the angular increment. As shown in Fig. 4 (top), the variance of the axial displacement estimates decreases with the maximum angle with the lowest value around 12°. Further increases in the maximum angle in the strain-tensor estimation algorithm produce a small increase in the variance. This is because the displacement noise has been reduced by the linear fitting procedure [22], [23] when using angular displacement estimates from small angles. The slight increase in the variance for maximum angles greater than 12° is due to the presence of increased noise at the larger insonification angles, as described in Fig. 2. To improve the efficiency

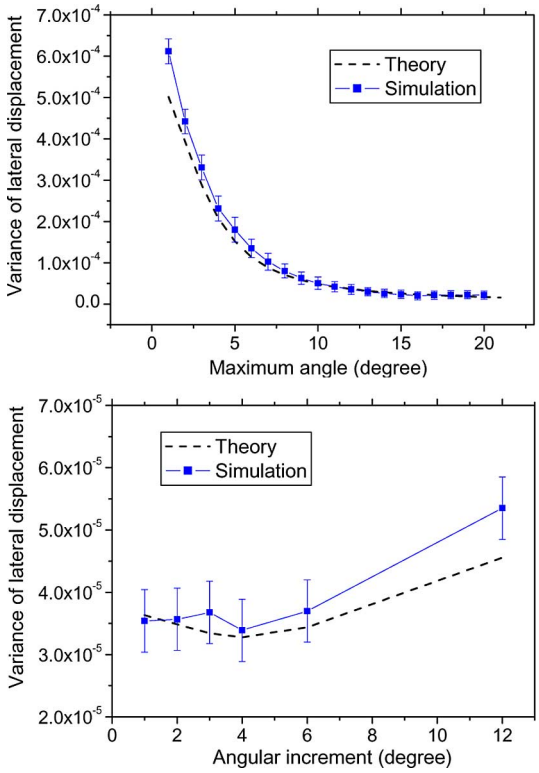

Fig. 4. Theoretical and simulation results for the variance of the axial displacement as a function of (top) the maximum angle and (bottom) the angular increment. The angular increment used in the plot on the top was 1° and the maximum angle used in the plot at the bottom was 12°.

of the strain-tensor estimation technique, we need to choose an optimum angular increment so that fewer angular displacements are required to obtained similar strain-tensor images. Angular increments of 1°–6° provide similar results for the variance of the axial displacement for a maximum angle of 12°, as shown in Fig. 4 (bottom). This is because RF data from a phantom volume scanned with beams separated by a small angular increment are highly correlated [30].

Fig. 5 presents a comparison between theoretical and simulation results for the variance of the lateral displacement as a function of the maximum angle and the angular increment. The angular increment used in the plot on the top was 1°, and the maximum angle used in the plot at the bottom was 12°. For the simulation results, the variances were computed over a rectangular ROI with dimensions of 1 (width) × 4 mm (height) at the center of axial displacement images. As illustrated in the figure, the variance of the lateral displacement is about two orders of magnitude higher than the variance of the axial displacement, as shown in Fig. 4. The theoretical curves exhibit a similar trend as the simulation results. The numerical discrepancies between theory and simulation results can be explained in a manner similar to that described earlier for the axial displacement results.

Fig. 6 presents examples of axial (top) and lateral (bottom) strain images of the simulated uniform phantom obtained using the strain-tensor estimation algorithm [22], [23]. As shown in Fig. 6(a)–(c), the image quality of the axial and lateral strains

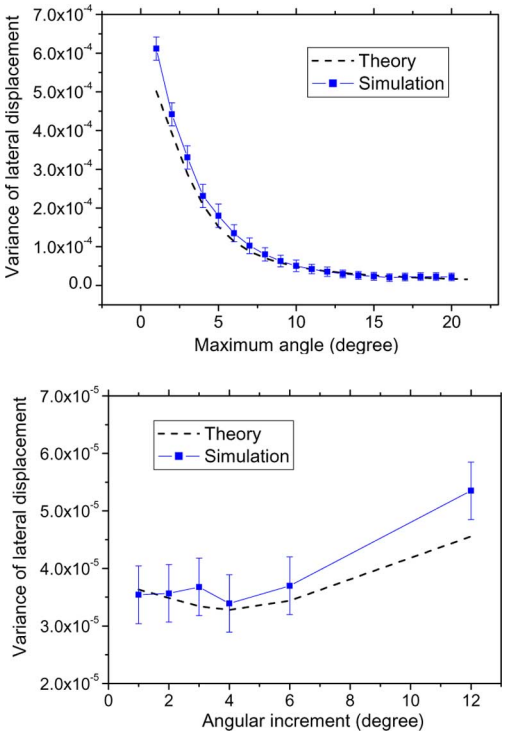

Fig. 5. Theoretical and simulation results for the variance of the lateral displacement as a function of (top) the maximum angle and (bottom) the angular increment. The angular increment used in the plot on the top was 1° and the maximum angle used in the plot at the bottom was 12°.

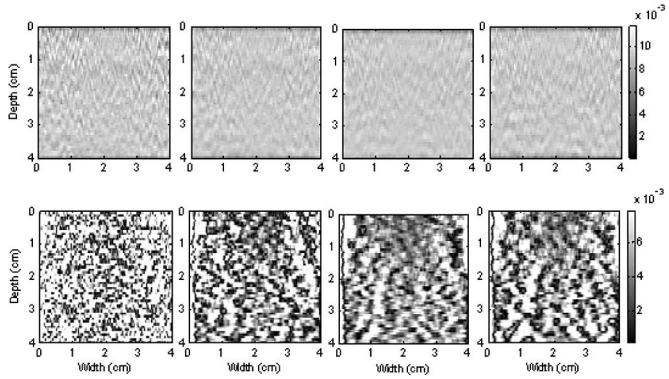

Fig. 6. Axial and lateral strain images obtained using different values of maximum angle and angular increment. (a) $\theta_{\max} = 3°$, $\Delta\theta = 1°$. (b) $\theta_{\max} = 9°$, $\Delta\theta = 1°$. (c) $\theta_{\max} = 15°$, $\Delta\theta = 1°$. (d) $\theta_{\max} = 15°$, $\Delta\theta = 3°$.

has been improved by using the larger maximum angles. Note that there is a slight decrease in the image quality when using an angular increment of 3° when compared to 1°, as shown in Fig. 6(c) and (d).

To quantitatively evaluate the effect of the maximum angle and angular increment on the image quality of the axial and lateral strains, the SNRe (see the Appendix A) was computed over a rectangular ROI of 1 × 1 cm at the center of the strain images and compared to theoretical predictions, as shown in Figs. 7 and 8. For the axial strain, theoretical curves show similar trends as the simulation results. The optimal value for the maximum angle is around 10°–12°, where the SNRe starts to

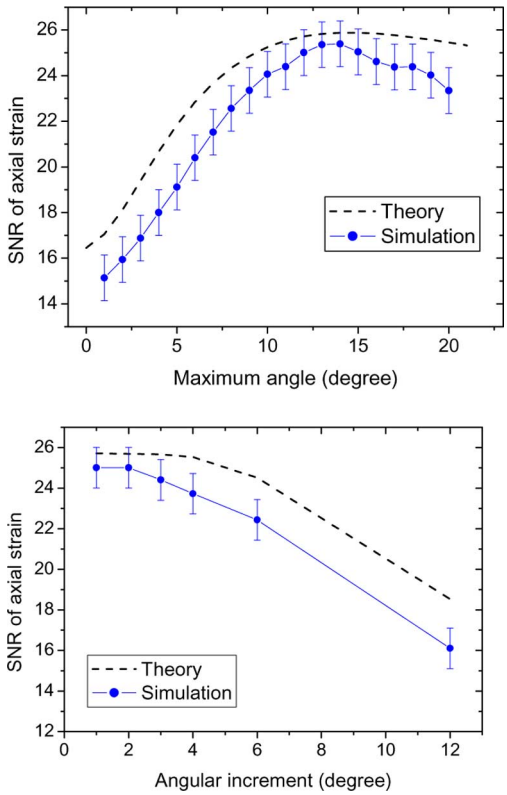

Fig. 7. Comparison between theoretical prediction and simulation results of the SNRe variation for axial strain estimates versus (top) the maximum angle and (bottom) the angular increment.

saturate and does not increase much with further increases in the maximum angle. For a fixed maximum angle of 12°, the optimal angular increment is around 4°, as shown in Fig. 7 (right). In general, smaller angular increments require a larger number of angular datasets to be acquired. So, the angular increment of 4° provides the best tradeoff in image quality versus acquisition time because fewer angular datasets are needed to obtain similar SNRe in the axial strain images.

For the lateral strain, the simulation results indicate that the SNRe increases with the maximum angle, reaching a maximum around 17°, and slightly decreases beyond this maximum angle, as shown in Fig. 8. The theoretical curve, however, increases all the way with the maximum angle, and follows a similar trend when the maximum angle is smaller than 17°, but overestimates the SNRe at larger maximum angles. This is because the theory underestimates the variance of the angular displacement, especially at large beam angles, as shown in Fig. 2. So, the optimal value for the maximum angle is around 15°–17° for lateral strain imaging. Note that the theory is less reliable at large beam angles. For a fixed maximum angle of 12°, the optimal angular increment is around 4°–6°, as shown in Fig. 8. From Figs. 7 and 8, note that the optimal parameters for the strain-tensor estimation model is different for axial strain and lateral strain imaging. Typically, the optimal parameter values of the maximum angle and angular increment are larger for lateral strain imaging when compared to that for axial strain imaging.

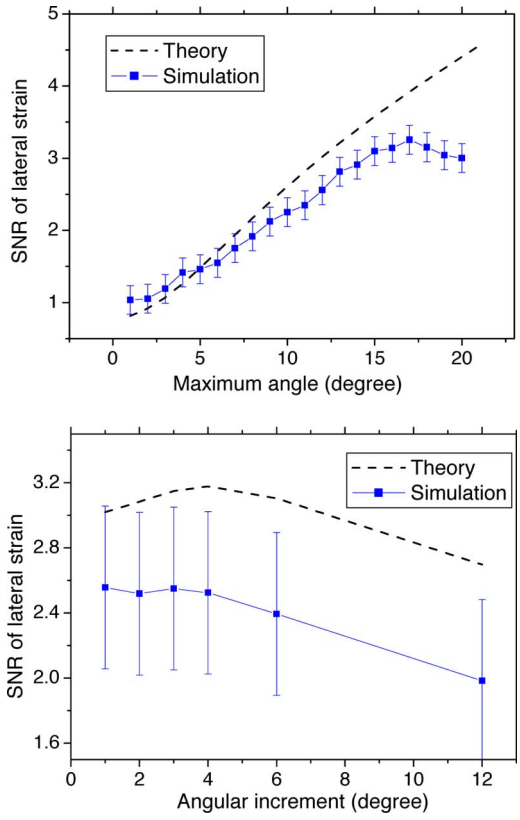

Fig. 8. Comparison between theoretical prediction and simulation results of the SNRe variation for the lateral strain estimates versus (top) the maximum angle and (bottom) the angular increment.

IV. Discussions

Utilizing RF data acquired from multiple beam insonification angles, the angular strain-tensor estimation method estimates the normal and shear strain images, but at the expense of additional processing time for local displacement estimations along the angular directions. It is important to choose appropriate values of the maximum angle and angular increment to achieve optimal performance with this technique. The theoretical derivation presented in this paper provides a method to predict the SNRe of the axial and lateral strain estimates as a function of the maximum angle and the angular increment. The comparison between the theoretical prediction and simulation results demonstrates that our theoretical model is capable of predicting the optimal parameters for the strain-tensor estimation method when the beam angle is smaller than 15°, as shown in Figs. 7 and 8. Although there are some discrepancies between theoretical and simulation results, the trend in the variation of the SNRe as a function of the maximum angle and angular increment is similar, which provides sufficient information to determine the optimal values for the maximum angle and the angular increment. The SNRe of the strain images also depends on other system parameters, such as the center frequency, bandwidth, aperture size, etc. It is therefore necessary to understand how all these system factors affect the optimal parameters for the strain-tensor estimation technique.

Fig. 9 shows the theoretical prediction of the SNRe of the axial and lateral strains as a function of the maximum angle and

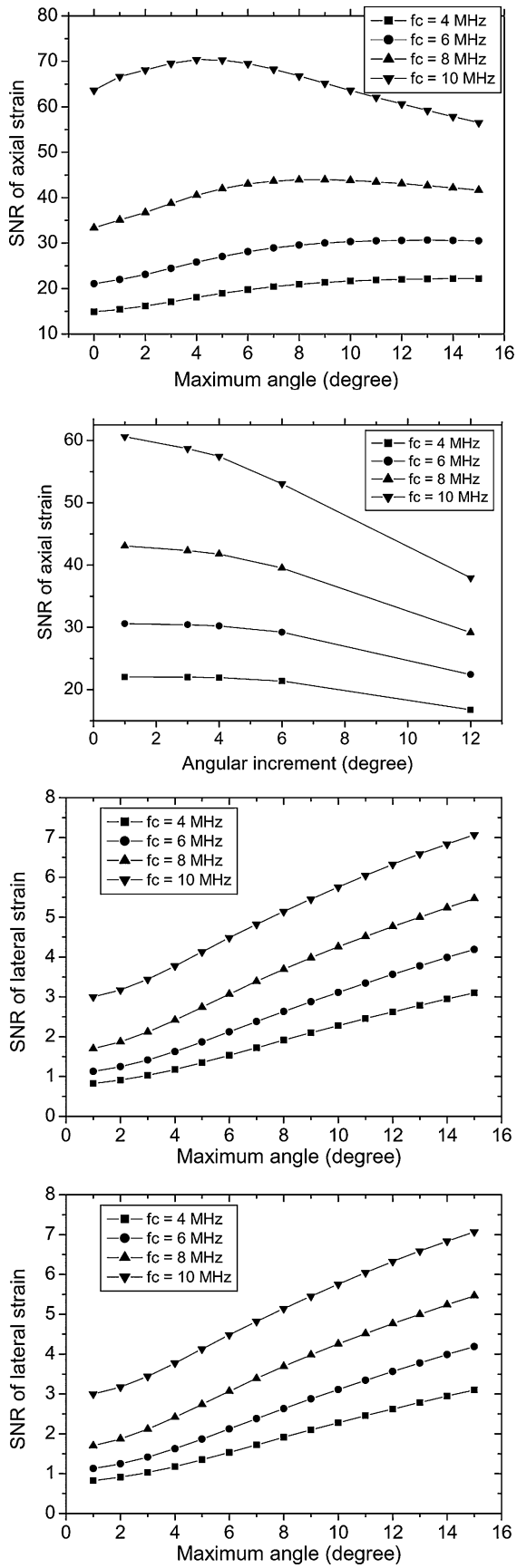

Fig. 9. Variations in the SNRe of the axial and lateral strain estimates versus the maximum angle and the angular increment for different center frequencies.

angular increment for different center frequencies. Results were obtained using 3-mm RF segments centered at a depth of 3 cm for a 1% applied compression. The aperture of the transducer was assumed to be 1.5 cm, and the bandwidth was 60%. As illustrated in the figure, higher center frequencies provide higher SNRe for the axial and lateral strain estimates. For the axial strain, the optimal values for the maximum angle and angular increment are smaller for higher center frequencies. The optimal acquisition scheme for a 10-MHz center frequency is to use a maximum angle of around 3° with an angular increment around 1° or smaller. At a center frequency of 4 MHz, however, a maximum angle of 10° with an increment of 5° is a good choice. This is because the echo signal decorrelates faster with beam angle at higher center frequencies due to the narrower beam width, as described in our previous work [24], [27]. The faster decorrelation between pre- and postcompression RF signals with beam angle at higher center frequencies, as given in (13), leads to increased noise artifacts in the angular displacement estimates with beam angle. Thus, the SNRe of the axial strain estimates begin to decrease at small beam angles. Similarly, the correlation between RF signals acquired from two different angles, as given in (14)–(16), decreases with the rotation angle (the difference between the two angles) and is faster at higher center frequencies. Therefore, the angular increment should be smaller when higher values of the center frequency are used. For lateral strain estimation, as shown in Fig. 9, the curves exhibit similar trends for all center frequencies. In other words, the center frequency has little effect on the optimal scheme for lateral strain estimation. The optimal value for the maximum angle should be chosen as large as possible, say 15°, for all center frequencies. Note that we should be careful, especially at higher center frequencies, since our theoretical model is not reliable at large beam angles, as described in Fig. 8.

Fig. 10 shows the theoretical prediction of the variation in the SNRe of the axial and lateral strains as a function of the maximum angle and angular increment for different aperture sizes. The RF segment studied here is again centered at a 3-cm depth with 1% strain, and the segment length is 3 mm. The insonification frequency used is 4 MHz. As illustrated in the figure, generally, smaller aperture sizes provide higher SNRe values for strain images. This is because the RF signals decorrelate faster with beam angle for larger aperture sizes due to narrower beam generated with larger apertures [24], which leads to increased noise artifacts in angular displacement and subsequently the strain images. Since the noise in the angular displacement estimates increases quickly with beam angle for larger aperture sizes, the optimal value of the maximum angle for axial strain estimation is very small, say 0° for aperture size of 20 mm, as shown in Fig. 10.

For lateral strain estimation, the SNRe increases with the maximum angle almost linearly, and the slope is smaller for larger aperture sizes due to the faster increase in the noise artifacts in the angular displacement estimates with beam angle. Note that the SNRe of the lateral strain is higher for large aperture sizes when the maximum angle is small (<4°), as shown in Fig. 10. The explanation for this behavior is that at small beam angles, the effect of aperture size on the variance of the

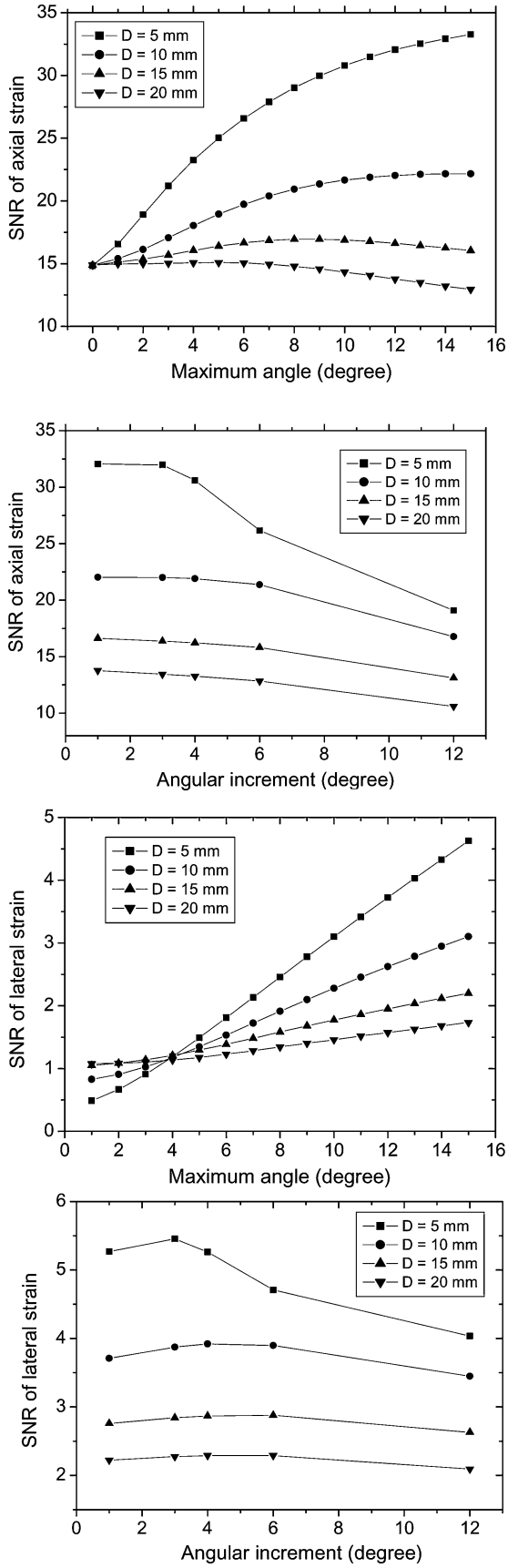

Fig. 10. Variation in the SNRe of the axial and lateral strains estimates versus the maximum angle and the angular increment for different aperture sizes.

lateral displacement estimates is primarily from the negative terms in (9b), which have larger magnitudes for large aperture sizes, since ρ_{ij} in (10) increases with aperture size [27]. As shown in Fig. 10, the optimal value for the angular increment should be smaller for small aperture sizes. This is because the correlation coefficient between RF signals acquired from the two angles, ρ_{ij} in (10), falls off quickly with rotation angle for smaller apertures [27].

The analysis in this paper assumes that tissue remains stationary during the pre- and postcompression imaging periods when RF data from different beam angles are recorded. In practice, however, tissue motion may occur during angular data acquisition procedure, and can introduce additional errors into the strain-tensor estimation technique, especially with free-hand compression. To minimize tissue motion during acquisition of the pre- and postcompression datasets, we utilize stepper-motor-controlled compression devices, as described in [23], which also reduces transducer movement during data acquisition. It is also desirable to use a smaller number of angles by choosing optimal values of the maximum angle and angular increment to speed up the angular data acquisition procedure, thereby reducing the impact of motion artifacts.

V. Conclusion

We have derived a theoretical expression for the variance of the axial and lateral displacement estimates, obtained using our strain-tensor estimation technique from data acquired at different insonification angles. This study is based on our previously derived theoretical model [24], [27], where the analysis of the correlation between pre- and postcompression RF echo signals obtained with an angular beam and the correlation between RF signals acquired from two different angles were presented. Under certain approximations, a closed-form analytical expression for the SNRe of the axial and lateral strains can be derived. However, for large beam angles ($>15^\circ$), tracking errors in the angular displacement estimation and the effective aperture change during the beam-steering procedure should also be taken into consideration in the theoretical model. This is beyond the scope of this study. The theoretical prediction matches well with numerical simulations presented in the paper. Note that in this study, numerical simulation was performed for 1% applied compression with the 1-D cross-correlation method used to track displacement along each insonification angle. For larger compressions, however, increased lateral motions are expected, and 2-D tracking algorithms should be used to estimate the angular displacement. For typical system parameters, the optimal maximum beam angle is around 10° for axial strain estimation and around 15° for lateral strain estimation. The optimal angular increment is around 4°–6°, which indicates that only five to seven beam angles are required for this strain-tensor estimation technique. Generally, the optimal value of the maximum angle for lateral strain estimation is larger than that for axial strain estimation. And the optimum angular increment should be smaller for high center frequencies and smaller aperture sizes. The theory presented in this paper is useful for choosing the optimum parameters for the angular data acquisition process in the strain-tensor estimation model.

Appendix A

The elastographic SNR of strain estimates:

$$\mathrm{SNR}_e = \frac{\varepsilon_s}{\sigma_s} \tag{A1}$$

where ε_s and σ_s are, respectively, the mean and standard deviation of the strains over a region of uniform elasticity.

References

[1] J. Ophir, I. Cespedes, H. Ponnekanti, Y. Yazdi, and X. Li, "Elastography—A quantitative method for imaging the elasticity of biological tissues," *Ultrason. Imaging*, vol. 13, pp. 111–134, Apr. 1991.

[2] B. S. Garra, E. I. Cespedes, J. Ophir, S. R. Spratt, R. A. Zuurbier, C. M. Magnant, and M. F. Pennanen, "Elastography of breast lesions: Initial clinical results," *Radiology*, vol. 202, pp. 79–86, Jan. 1997.

[3] T. Varghese, J. A. Zagzebski, and F. T. Lee, "Elastographic imaging of thermal lesions in the liver *in vivo* following radiofrequency ablation: Preliminary results," *Ultrasound Med. Biol.*, vol. 28, pp. 1467–1473, Nov./Dec. 2002.

[4] E. S. Burnside, T. J. Hall, A. M. Sommer, G. K. Hesley, G. A. Sisney, W. E. Svensson, J. P. Fine, J. J. Jiang, and N. J. Hangiandreou, "Differentiating benign from malignant solid breast masses with US strain imaging," *Radiology*, vol. 245, pp. 401–410, Nov. 2007.

[5] M. Sumura, K. Shigeno, T. Hyuga, T. Yoneda, H. Shiina, and M. Igawa, "Initial evaluation of prostate cancer with real-time elastography based on step-section pathologic analysis after radical prostatectomy: A preliminary study," *Int. J. Urol.*, vol. 14, pp. 811–816, Sep. 2007.

[6] M. A. Hobson, M. Z. Kiss, T. Varghese, A. M. Sommer, M. A. Kliewer, J. A. Zagzebski, T. J. Hall, J. Harter, E. M. Hartenbach, and E. L. Madsen, "*In vitro* uterine strain imaging—Preliminary results," *J. Ultrasound Med.*, vol. 26, pp. 899–908, Jul. 2007.

[7] D. M. Regner, G. K. Hesley, N. J. Hangiandreou, M. J. Morton, M. R. Nordland, D. D. Meixner, T. J. Hall, M. A. Farrell, J. N. Mandrekar, W. S. Harmsen, and J. W. Charboneau, "Breast lesions: Evaluation with US strain imaging—Clinical experience of multiple observers," *Radiology*, vol. 238, pp. 425–437, Feb. 2006.

[8] R. L. Maurice, M. Daronat, J. Ohayon, E. Stoyanova, F. S. Foster, and G. Cloutier, "Non-invasive high-frequency vascular ultrasound elastography," *Phys. Med. Biol.*, vol. 50, pp. 1611–1628, Apr. 2005.

[9] T. Varghese, J. Ophir, E. Konofagou, F. Kallel, and R. Righetti, "Tradeoffs in elastographic imaging," *Ultrason. Imaging*, vol. 23, pp. 216–248, Oct. 2001.

[10] J. Ophir, F. Kallel, T. Varghese, M. Bertrand, I. Cespedes, and H. Ponnekanti, "Elastography: A systems approach," *Int. J. Imaging Syst. Technol.*, vol. 8, pp. 89–103, 1997.

[11] A. H. Quazi, "An overview on the time-delay estimate in active and passive systems for target localization," *IEEE Trans. Acoust. Speech Signal Process.*, vol. ASSP-29, no. 3, pp. 527–533, Jun. 1981.

[12] F. Kallel and J. Ophir, "Three-dimensional tissue motion and its effect on image noise in elastography," *IEEE Trans. Ultrason. Ferroelectr. Freq. Control*, vol. 44, no. 6, pp. 1286–1296, Nov. 1997.

[13] M. Bilgen, "Dynamics of errors in 3D motion estimation and implications for strain-tenser imaging in acoustic elastography," *Phys. Med. Biol.*, vol. 45, pp. 1565–1578, Jun. 2000.

[14] M. O'Donnell, A. R. Skovoroda, B. M. Shapo, and S. Y. Emelianov, "Internal displacement and strain imaging using ultrasonic speckle tracking," *IEEE Trans. Ultrason. Ferroelectr. Freq. Control*, vol. 41, no. 3, pp. 314–325, May 1994.

[15] F. Kallel and M. Bertrand, "Tissue elasticity reconstruction using linear perturbation method," *IEEE Trans. Med. Imag.*, vol. 15, no. 3, pp. 299–313, Jun. 1996.

[16] M. A. Lubinski, S. Y. Emelianov, K. R. Raghavan, A. E. Yagle, A. R. Skovoroda, and M. O'Donnell, "Lateral displacement estimation using tissue incompressibility," *IEEE Trans. Ultrason. Ferroelectr. Freq. Control*, vol. 43, no. 2, pp. 247–256, Mar. 1996.

[17] E. Konofagou and J. Ophir, "A new elastographic method for estimation and imaging of lateral displacements, lateral strains, corrected axial strains

and Poisson's ratios in tissues," *Ultrasound Med. Biol.*, vol. 24, pp. 1183–1199, Oct. 1998.
[18] Y. G. Fung, *Biomechanical Properties of Living Tissues*. New York: Springer-Verlag, 1981.
[19] J. S. Jurvelin, M. D. Buschmann, and E. B. B. Hunziker, "Mechanical anisotropy of the human knee articular cartilage in compression," in *Proc. Inst. Mech. Eng. [H]*, 2003, vol. 217, pp. 215–219.
[20] E. E. Konofagou, T. P. Harrigan, J. Ophir, and T. A. Krouskop, "Poroelastography: Imaging the poroelastic properties of tissues," *Ultrasound Med. Biol.*, vol. 27, pp. 1387–1397, Oct. 2001.
[21] R. Righetti, J. Ophir, S. Srinivasan, and T. A. Krouskop, "The feasibility of using elastography for imaging the Poisson's ratio in porous media," *Ultrasound Med. Biol.*, vol. 30, pp. 215–228, Feb. 2004.
[22] U. Techavipoo, Q. Chen, T. Varghese, and J. A. Zagzebski, "Estimation of displacement vectors and strain tensors in elastography using angular insonifications," *IEEE Trans. Med. Imag.*, vol. 23, no. 12, pp. 1479–1489, Dec. 2004.
[23] M. Rao, Q. Chen, H. Shi, T. Varghese, E. L. Madsen, J. Zagzebski, and T. A. Wilson, "Normal and shear strain estimation using beam steering on linear-array transducers," *Ultrasound Med. Biol.*, vol. 33, pp. 57–66, 2007.
[24] M. Rao and T. Varghese, "Correlation analysis of the beam angle dependence for elastography," *J. Acoust. Soc. Amer.*, vol. 119, pp. 4093–4101, 2006.
[25] L. L. Scharf, "Least squares," in *Statistical Signal Processing: Detection, Estimation, and Time Series Analysis*. Reading, MA: Addison-Wesley, 1991, pp. 359–415.
[26] T. Varghese and J. Ophir, "A theoretical framework for performance characterization of elastography: The strain filter," *IEEE Trans. Ultrason. Ferroelectr. Freq. Control*, vol. 44, no. 1, pp. 164–172, Jan. 1997.
[27] M. Rao and T. Varghese, "Correlation analysis for angular compounding in strain imaging," *IEEE Trans. Ultrason. Ferroelectr. Freq. Control*, vol. 54, no. 9, pp. 1903–1907, Sep. 2007.
[28] Y. D. Li and J. A. Zagzebski, "A frequency domain model for generating B-mode images with array transducers," *IEEE Trans. Ultrason. Ferroel. Freq. Control*, vol. 46, no. 3, pp. 690–699, May 1999.
[29] M. Rao and T. Varghese, "Spatial angular compounding for elastography without the incompressibility assumption," *Ultrason. Imaging*, vol. 27, pp. 256–270, 2005.
[30] P. He, "Spatial compounding in 3D imaging of limbs," *Ultrason. Imaging*, vol. 19, pp. 251–265, Oct. 1997.

Min Rao (S'06) was born in Anqing, China, in 1977. She received the B.E. and Ph.D. degrees in electrical engineering from Southeast University, Nanjing, China, in 1999 and 2004, respectively, and the M.S. and Ph.D. degrees in medical physics from the University of Wisconsin, Madison, in 2007 and 2008, respectively.

She is currently with the University of Wisconsin, Madison. Her current research interests include elastography, computer modeling in ultrasound imaging, and signal and image processing applications in medical imaging.

Tomy Varghese (S'92–M'95–SM'00) received the B.E. degree in instrumentation technology from the University of Mysore, Mysore, India, in 1988, and the Ph.D. degree in electrical engineering from the University of Kentucky, Lexington, in 1995.

From 1995 to 2000, he was a Postdoctoral Research Associate with the Ultrasonics Laboratory, Department of Radiology, University of Texas Medical School, Houston. He is currently an Associate Professor in the Department of Medical Physics, University of Wisconsin, Madison. His current research interests include elastography, ultrasound imaging, ultrasonic tissue characterization, detection and estimation theory, statistical pattern recognition, and signal and image processing applications in medical imaging.

Dr. Varghese is a Senior Member of the American Institute of Ultrasound in Medicine (AIUM), and a member of the American Association of Physicists in Medicine (AAPM) and the Eta Kappa Nu.